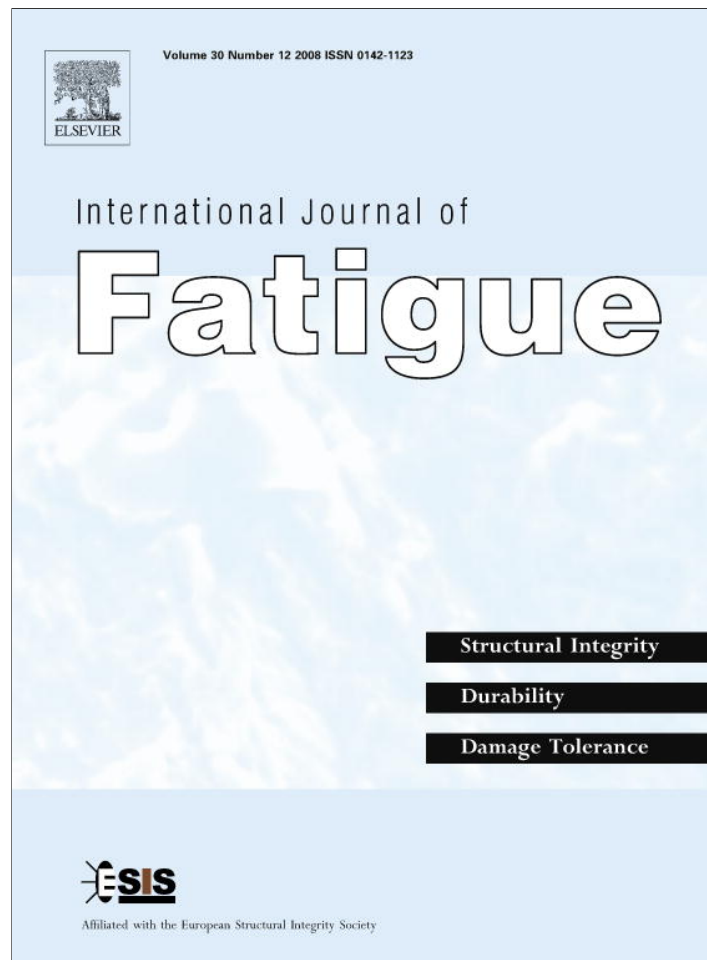


Provided for non-commercial research and education use.  
Not for reproduction, distribution or commercial use.



This article appeared in a journal published by Elsevier. The attached copy is furnished to the author for internal non-commercial research and education use, including for instruction at the authors institution and sharing with colleagues.

Other uses, including reproduction and distribution, or selling or licensing copies, or posting to personal, institutional or third party websites are prohibited.

In most cases authors are permitted to post their version of the article (e.g. in Word or Tex form) to their personal website or institutional repository. Authors requiring further information regarding Elsevier's archiving and manuscript policies are encouraged to visit:

<http://www.elsevier.com/copyright>



Contents lists available at ScienceDirect

## International Journal of Fatigue

journal homepage: [www.elsevier.com/locate/ijfatigue](http://www.elsevier.com/locate/ijfatigue)

## A cold dwell fatigue crack nucleation criterion for polycrystalline Ti-6242 using grain-level crystal plasticity FE Model

Kedar Kirane<sup>1</sup>, Somnath Ghosh<sup>2,\*</sup>

Department of Mechanical Engineering, The Ohio State University, Room W496, Scott Laboratory, 201 West 19th Avenue, Columbus, OH 43210, USA

## ARTICLE INFO

## Article history:

Received 7 March 2008

Received in revised form 26 May 2008

Accepted 29 May 2008

Available online 13 June 2008

## Keywords:

Ti-6242

Crack initiation

Dislocation pileup

Dwell fatigue

Crystal plasticity

## ABSTRACT

A grain-level fatigue crack nucleation criterion for cold dwell in Ti-6242 alloy is developed in this paper using a rate and size dependent anisotropic elasto-crystal plasticity constitutive model, and validated with experiments. Early crack initiation in Ti-6242 under cold dwell fatigue has been identified to be caused by stress concentrations in a hard grain, induced by load shedding from creep in adjacent soft grains. Accurate prediction of local stress and strain evolution during loading requires a robust representation of morphological and crystallographic features of the microstructure. These are accounted for in the FE model in a statistically equivalent sense. The proposed crack nucleation model is based on the observed similarities between crack evolution at the tip of a crack and a dislocation pileup. The nucleation model is calibrated and validated using data available from acoustic microscopy though real time monitoring of crack evolution in dwell fatigue experiments.

© 2008 Elsevier Ltd. All rights reserved.

### 1. Introduction

Many of the widely used fatigue life techniques, such as the stress or strain life approaches are empirical and macroscopic in nature [1]. Most of them are phenomenological and do not account for the material microstructure or the interacting mechanisms at the microstructure level. As a result, many of them fail to predict crack initiation as well as the observed variation in fatigue lives with microstructure with precision [2]. A microstructure level crack nucleation model, motivated from the understanding of the microstructural mechanisms and their interactions, is necessary to develop robust predictive capability. With this motivation, this work attempts to develop a microstructural crack initiation criterion for the polycrystalline titanium alloy Ti-6242 under cyclic cold dwell loading conditions. Ti-6242 alloy, consisting of  $\alpha$ - $\beta$  phases, is widely used in aircraft engine components due to its desirable mechanical and structural properties. However, its premature failure under dwell loading has drawn significant research attention [3,4]. The dwell sensitivity of Ti-6242 has been attributed to local creep effects that occur during the hold period of dwell loading in [5].

Experimental studies using fractography and orientation imaging microscopy (OIM) images at failure sites have shown that the

failure site is faceted with no ductility in [6–8]. However a large amount of slip accumulation is observed around the failure site. These observations infer the occurrence of the time dependent stress redistribution between neighboring grains of different strengths. Time dependent load shedding, due to plastic strain accumulation in the neighboring soft grains, causes evolving stress concentration in a hard grain with higher slip system resistance. This load shedding behavior has been postulated to be responsible for crack initiation in Ti-6242 under dwell fatigue in [3,8]. Cyclic plasticity and fatigue failure in Ti alloys have been investigated at the microstructural level using computational crystal plasticity models in [9,10].

For computational modeling of the load shedding phenomenon, a rate and size dependent anisotropic elasto-crystal plasticity constitutive model that has been developed and experimentally validated in [11–14] is employed. The model does not account for diffusion-mediated mechanisms such as dislocation climb, since cold creep phenomenon occurs at temperatures lower than that at which diffusion-mediated deformation is expected (room temperature is about 15% of the homologous temperature for titanium). TEM studies [15] have shown that deformation actually proceeds via dislocation glide, where the dislocations are inhomogeneously distributed into planar arrays. In addition, twinning is not considered in this model, as it has been experimentally observed in [16] that twinning occurs in Ti alloys only with low Al content. As the Al content in Ti-6242 is  $\sim 6.01\%$ , no twinning is expected and plastic deformation is found to occur only due to slip accumulation in slip systems. Details of the model have been given [12,14]. For accurate capture of the complex local stress and strain

\* Corresponding author. Tel.: +1 614 292 2599; fax: +1 614 292 3163.

E-mail address: [ghosh.5@osu.edu](mailto:ghosh.5@osu.edu) (S. Ghosh).<sup>1</sup> Graduate Research Associate.<sup>2</sup> John B. Nordholt Professor.

evolutions during load shedding, critical microstructural features such as grain sizes and shapes and grain orientations are accounted for in the FE model in a statistically equivalent sense. Extensive techniques for generating 3D statistically equivalent FE models from 2D orientation images of FIB generated sections of a polycrystalline microstructure have been developed in [17,18]. In addition, a method of projecting 2D morphological and crystallographic data to statistically equivalent 3D microstructural images using weights that are derived from stereological projections of 2D statistical distribution functions has been developed in [19]. This method is used in this work to create 3D representative microstructures for simulation.

The crack nucleation model is based on evolving stresses in a grain, associated with dislocation pileups in neighboring grains. It is conceived from some of the dislocation pileup based nucleation models, proposed in the literature e.g. [20]. The model is calibrated using results and observations from crystal plasticity FE simulations of a variety of dwell fatigue experiments. The functional form of the crack nucleation due to load shedding is motivated from the equivalence between crack nucleation ahead of a dislocation pileup and crack evolution at a pre-existing crack tip. The nucleation criterion at a point in a grain depends on an effective stress measure on a slip system, as well as a length scale corresponding to the dislocation pileup in the neighboring grains. Using definitions of statistically stored and geometrically necessary dislocations [21], this length scale is shown to be a known function of the equivalent plastic strain and its gradient. Material constants analogous to fracture toughness are calibrated using dwell fatigue simulation data at critical failure sites. The simulation results are compared with experimental data from acoustic microscopy of crack monitoring in [4] for validation. Accurate predictive capabilities of the resulting model, in terms of number of cycles for crack initiation and also the location of crack initiation are demonstrated through a number of experimental validations.

## 2. Load shedding phenomenon in polycrystalline Ti-6242

### 2.1. Experimental observations

#### 2.1.1. Crack initiation site under dwell loading conditions

Extensive experimental studies on the relation between crack evolution and crystallographic orientations in samples of Ti-6242 have been conducted in [6] using quantitative tilt fractography and Electron Back Scattered Diffraction (EBSD) techniques in SEM. Fig. 1 shows a fractograph of a small region of crack initiation site for a failed Ti-6242 sample in dwell fatigue. The failure site is found to consist of facets that form on the basal plane of the primary  $\alpha$  grains (*hcp*). They predominantly lie on a plane perpendicular to the principal tensile loading direction [6–8]. It has been observed in [22] that the angle between the loading axis and the 'c'-axis, i.e. the 'c'-axis orientation ( $\theta_c$ ) of the grains at the failure site is quite small ( $\sim 0$ – $30^\circ$ ). Furthermore, the failure site shows a low prism activity with Schmid factor (*SF*)  $\sim 0$ – $0.1$  and a moderate basal activity with a *SF*  $\sim 0.3$ – $0.45$ . However, the region surrounding the failure site has a high prismatic and basal activity with a *SF*  $\sim 0.5$ . Thus, it may be inferred that while crack initiation occurs in a region that is unfavorably oriented for slip, it is surrounded by grains that are favorably oriented for slip. In other words, crack initiates in a hard-orientation grain surrounded by soft-orientation grains. The observations suggest time dependent accumulation of stress in hard oriented grains due to load shedding with increasing plastic deformation in the surrounding soft grains, which is responsible for crack initiation in alloys like Ti-6242 under creep and dwell loading.

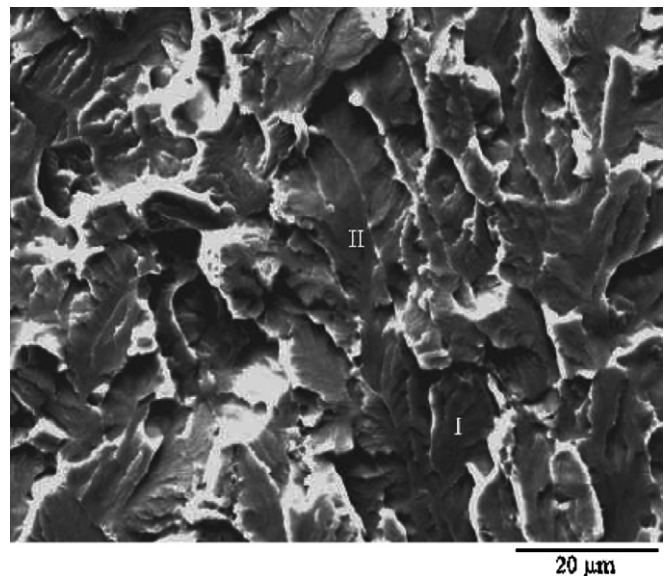


Fig. 1. Fractograph of a faceted initiation site for a failed Ti-6242 dwell fatigue sample [7].

#### 2.1.2. Crack detection and monitoring in mechanical tests on Ti-6242

Ultrasonic techniques, such as in situ surface acoustic wave techniques have been developed for monitoring the subsurface phenomenon of crack initiation [3,4], which have been applied to high micro-texture  $\alpha/\beta$  forged Ti-6242 samples in [4,23] for dwell fatigue and creep experiments. The experiments monitored crack initiation and growth in real time, thus making estimation of the time for crack initiation possible. Three dwell fatigue experiments from this set are considered as references in the present study. The microstructures of the samples in the three experiments are labeled as MS1, MS2 and MS3.

Each trapezoidal dwell cycle in the dwell tests has a maximum applied traction (load) of 869 MPa at a hold time of 2 min, and a loading/unloading time of 1 s. The value of maximum applied load corresponds to 95% of the macroscopic yield stress of the material [4]. The stress ratio, measured as the ratio of the minimum to maximum load, is zero. In [4,23] crack growth in samples MS2 and MS3 is monitored through micro-radiographic images taken by interrupting the experiment every 15 cycles. An ultrasonic modulation technique, which can enhance the strength of the crack generated ultrasonic signal, has been implemented for better crack detection. It involves application of a small modulation load for 5–10 s at the maximum, minimum and average loads during the loading and unloading part. The small magnitude of the modulation load is not expected to affect the dwell fatigue response of the samples [4]. Fig. 2 is a sample plot of the observed crack length as a function of the number of cycles for a secondary crack in the MS2 sample. This crack is of length 125  $\mu\text{m}$  at 625 cycles, while at 663 cycles, it is of length 470  $\mu\text{m}$ . Extrapolating backwards to zero length as shown in Fig. 2, the number of cycles to crack initiation for this crack is estimated to be approximately 530. Similarly, the number of cycles to crack initiation is determined for all cracks in MS2 and MS3. The crack initiation cycles extrapolated from the plots for the primary cracks, i.e. the crack grew to cause final failure, are given in the Table 1. It can be seen that the primary crack initiated at 83% life (550 cycles) for the MS2 sample, while it initiated at 85% life (380 cycles) for the MS3 sample. The results in [4] generally suggest that primary crack initiation in dwell fatigue occurs in the range 80–90% of total number of cycles to failure.

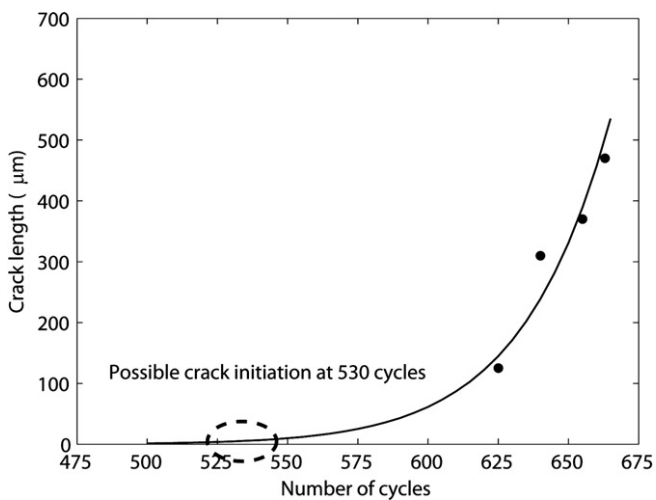


Fig. 2. Crack length as a function of number of cycles for a secondary crack in the microstructure MS2.

Table 1  
Primary crack initiation data in dwell fatigue experiments on Ti-6242 by ultrasonic monitoring

Microstructure label	Test type	Sample life	Time to primary crack initiation (from ultrasonic monitoring)	% Life at primary crack initiation
MS1	2-Min dwell load	352 cycles	–	–
MS2	2-Min dwell load (with modulation)	663 cycles	550 cycles	83
MS3	2-Min dwell load (with modulation)	447 cycles	380 cycles	85

2.2. Finite element modeling of the load shedding phenomenon

2.2.1. The crystal plasticity based FE model

Ti-6242 is a biphasic polycrystalline alloy with a highly anisotropic microstructure with colonies of transformed  $\beta$  phase in a matrix of primary  $\alpha$  grains. The alloy considered in this study consists of 70% primary  $\alpha$  and 30% transformed  $\beta$  grains. The primary  $\alpha$  phase consists of equi-axed grains with an *hcp* structure whereas the transformed  $\beta$  colonies have alternating  $\alpha$  (*hcp*) and  $\beta$  (*bcc*) laths. To incorporate the effect of various microstructural parameters, a size and time dependent large strain crystal plasticity based finite element model has been systematically developed in [12–14,24]. The model incorporates a rate dependent anisotropic elastocrystal plasticity constitutive model for the different phases in this material. Tension–compression asymmetry is accounted for in the slip system variables and a homogenized model of the  $\alpha + \beta$  phase colony regions in the Ti-6242 microstructure has been developed. To account for size effect, a Hall-Petch type relation for size dependent initial deformation resistance with various characteristic length scales, depending on the slip direction, is incorporated in the model [14,24]. Material properties for each of the constituent phases and slip systems in the crystal plasticity model and the parameters in the size effect relationship are calibrated and provided in [12–14,24].

2.2.2. Image based statistical representation of actual microstructures

The importance of representing critical morphological and crystallographic features of the polycrystalline microstructures in the

accurate predictions of stress and strain localization and crack initiation has been emphasized in [14,19,24]. In the recent years, there have been significant advances in reconstruction and simulation of 3D polycrystalline microstructures based on information obtained from a dual beam Focused Ion Beam-Scanning Electron Microscope system (FIB-SEM). This system is able to acquire 3D orientation or electron backscatter diffraction (EBSD) data from a series of material cross-sections. This information has been successfully used in [17] for automatic segmentation of individual grains from the image and subsequently translated into a 3D mesh for FEA. Through a multitude of data sets, the distributions of microstructural parameters can be captured and accurately represented in the form of 3D microstructure reconstruction [18]. Computational tools have recently been developed in [19] to create 3D synthetic microstructures that yield 2D projected distributions, which are statistically equivalent to measured 2D OIM distributions of certain microstructural features. These microstructures are built by projecting 2D morphological and crystallographic data in the third dimension using weights derived from stereological projections of 2D statistical distribution functions. The synthetic microstructure generation method in [19] is used in this work to construct statistically equivalent finite element models to aid in the development of a microstructural crack initiation model.

The microstructures are created from observations of two specific sites in the material samples, viz. (i) a critical region, in the vicinity of a dwell fatigue failure, and (ii) a non-critical region, away from it. The first sample considered is MS1. Two orientation

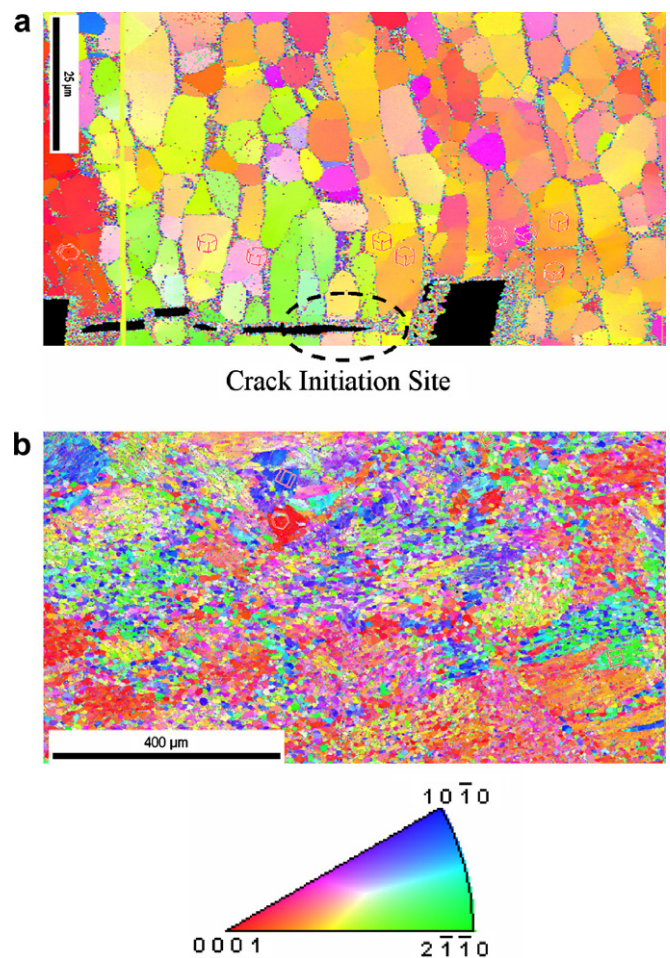


Fig. 3. OIM scans of (a) the critical primary crack initiation site and (b) a non-critical region away from crack in the MS1 microstructure.

imaging microscopy or OIM scans are performed on this sample; the first on a small critical region surrounding the primary crack tip as shown in Fig. 3a, while the second on a non-critical region away from the crack as shown in Fig. 3b. Two FE models of statistically equivalent simulated microstructures at the critical and non-critical regions are developed for analysis. In the development of the crack initiation model, it is expected that the initiation criterion will be met at some location in the critical FE model, but will not be satisfied in the non-critical FE model. These models are vital to test the sensitivity of the criterion to microstructural conditions.

The following steps are performed for the construction of 3D microstructures from 2D OIM scans at the critical and non-critical sites. As discussed in [18,19], statistical distribution functions of various microstructural parameters in the 2D OIM scan are generated and subsequently projected in the third dimension for creating the 3D statistics. The assumptions and process implemented to extract 3D statistics from the 2D distributions of morphological and crystallographic features are briefly outlined in this section and are described in [19].

- (i) *Distribution functions of grain size and shape*: Characterization of the 2D OIM scan involves measuring the aspect ratio, area and principal axes orientation of ellipses that are fit to grains in the scan. To determine the 3D size and shape distributions of the grains in the microstructure, an assumption made here is that grain sections in the 2D OIM scans have a similar size and shape correlation to their parent 3D structures, as elliptical sections through ellipsoidal 3D grains have to each other. A large number of ellipsoids of various sizes and

shapes are randomly sectioned and the resulting elliptical sections are recorded. Probabilistic weighting functions are created for the grain reconstruction process. The 3D ellipsoid that produces an elliptical section closest in shape and size to a 2D OIM grain scan is assumed to have a high probability in representing the corresponding 3D grain. An assumption is also needed for the orientation distribution of the ellipsoids relative to the sectioning plane of the OIM scan. In [19], three orthogonal sections have been taken to help determine this distribution. However, in this work, only one section of the surface scan is available, and the orientation distribution of the ellipsoids is assumed to be random. After the determination of the 3D size and shape distributions, a constrained Voronoi tessellation is executed for generating the grain shapes, with initial seed points at the centroid of the ellipsoids as discussed in [18,19]. Fig. 4a shows the distribution of 2D grain size observed in the scan, while the histogram of the reconstructed 3D grain size distribution is shown in Fig. 4b. The observed mismatch between 2D and 3D distributions is attributed to the fact that only one 2D section is used to construct the 3D model. Many of the grain sections in the OIM are not through the “center” of the grains and thus may appear smaller than the true grain size. This explains the shift of the mean of the 3D grain size distribution to the right in comparison with the 2D distribution.

- (ii) *Distribution of number of neighbors*: The reconstructed 3D grains are placed in a representative cubic volume with a constraint that each grain has appropriate number of neighbors, as determined by 3D projection of the 2D OIM scan,

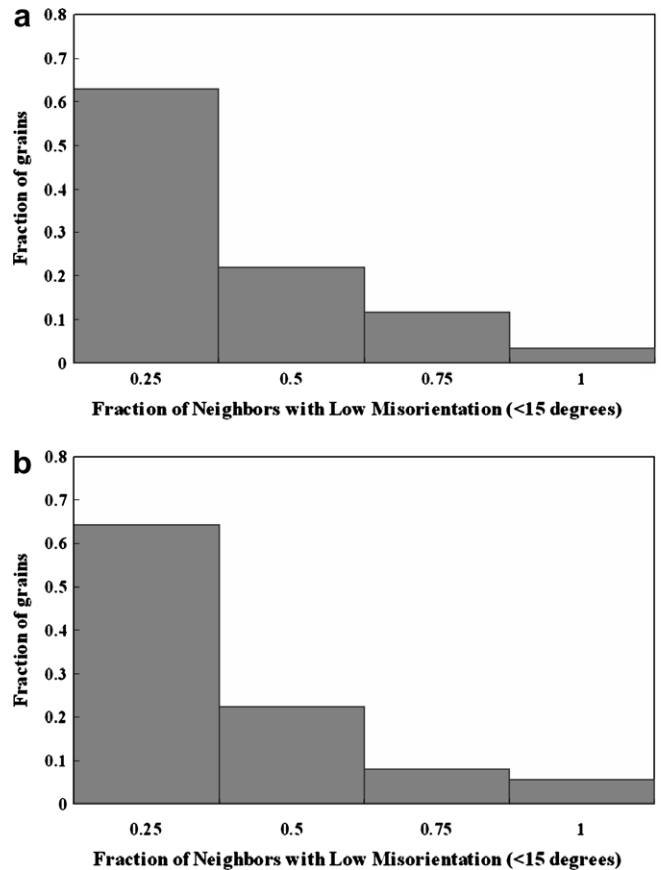
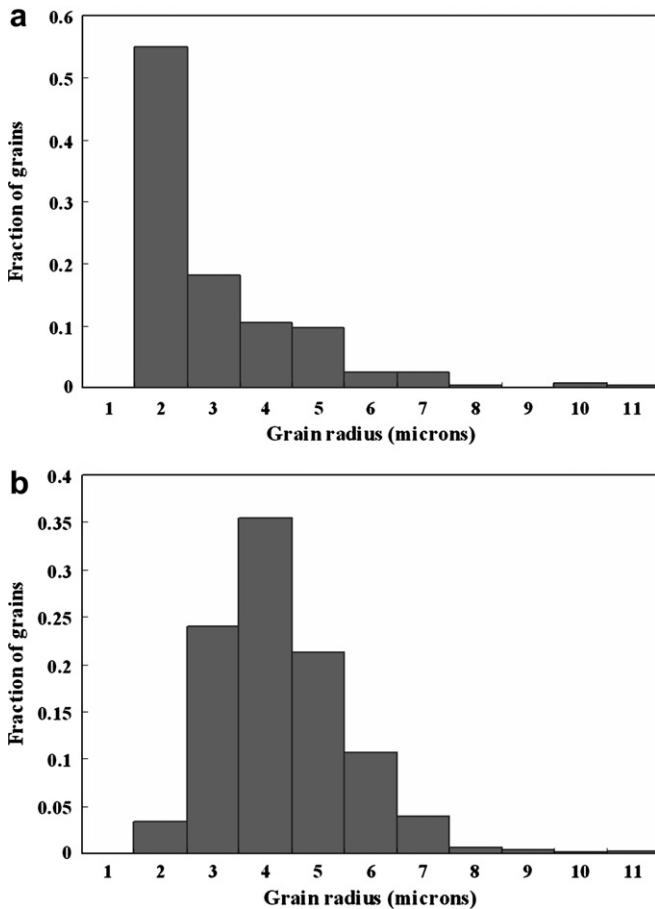


Fig. 4. Grain size distributions (a) from OIM scan of critical region of MS1 and (b) in the critical FE model.

Fig. 5. Micro-texture distributions (a) from OIM scan of critical region (b) in the critical FE model of MS1.

discussed in [19]. In the 2D OIM scan, grains have 3 to 12 neighbors depending on their size, while corresponding grains in the 3D representation have 8 to 25 neighbors. The representative cube for the MS1 microstructure has dimensions  $65\ \mu\text{m} \times 65\ \mu\text{m} \times 65\ \mu\text{m}$  and consists of 949 grains.

- (iii) *Distribution of crystallographic orientations*: The crystallographic orientation assignment to the grains in the cubic volume is executed by 3 major steps delineated as (a) Orientation probability assignment method (OPAM); (b) Misorientation probability assignment method (MPAM) and (c) Micro-texture probability assignment method (MTPAM). These are described in detail in [12,18]. Fig. 5 shows the micro-texture distribution in the 2D scan and in the 3D model, with satisfactory agreement.

The reconstructed 3D model has distributions of orientation, misorientation, micro-texture, grain size and number of neighbors that are statistically equivalent to those observed experimentally from the OIM scan. The model is subsequently discretized into a finite element mesh of 78,540 tetrahedron elements. The present 3D FE model is considered to be fairly representative of the microstructural characteristics in the critical and non-critical regions.

### 2.2.3. Mesh convergence study

Since local variables in the finite element simulations are pivotal to the development of the crack nucleation criterion, a sensitivity study of the local variables with respect to mesh density is done prior to the dwell fatigue analysis. The MS1 microstructure is used for this study with two different mesh densities. Both FE models have the same number of grains i.e. 949 and the same orientation, misorientation, micro-texture and grain size distributions. The first model consists of 78,540 elements while the second has 116,040 elements, which is approximately 150% higher in mesh density. A creep simulation is performed for both these models for 1000 s at an applied load of 869 MPa in the  $y$ -direction. The local stress component in the loading direction and the local plastic strain at the end of 1000 s are compared for various sections in the FE models. The stresses are found to be in good agreement

for the two models. Plots comparing the distribution of these variables along a section parallel to the  $x$ -axis, in Figs. 7a and b show excellent agreement between the two models. Results along other sections also confirm this agreement. These results indicate that the 78,540-element mesh is a converged mesh for the loading considered, and is henceforth used in this study for the development of the crack initiation criterion.

### 2.2.4. Load shedding simulation in polycrystalline Ti-6242

For a heuristic understanding of the effect of microstructure on the grain-to-grain load shedding behavior, a dwell fatigue FE simulation is performed for the microstructure of sample MS1, extracted from the critical region. The simulation is run for 352 cycles, which corresponds to the number of cycles to failure for the experiment. Each dwell cycle in the applied dwell loading has a maximum applied traction (load) of 869 MPa at a hold time of 2 min, and a loading/unloading time of 1 s. Simulation is conducted with the polycrystalline FE model shown in Fig. 6, where the time dependent dwell loading is applied in the form of a uniform tensile load on the  $Y = 65\ \mu\text{m}$  face of the model in the  $Y$ -direction.

Results of the simulations are shown in Fig. 8a and compared with morphological variations in Fig. 8b. Fig. 8a plots the local stress  $\sigma_{22}$  after 1 cycle and 300 cycles respectively, along a section A–A in Fig. 6, which passes through a hard–soft grain combination as shown in the prominent SF plot of Fig. 8b. In Fig. 8a, there is a stress peak at point X and stress valley at point Y. The stress peak at X at 300 cycles is considerably higher than that at 1 cycle, and much higher than the applied stress. The peak stress rises with time while the valley drops with time as a result of load shedding caused by plastic strain in the neighborhood of X. The prismatic SF is seen to be the prominent SF for this section as shown in Fig. 8b. Points X and Y, where maximum variation in stress profile is seen, have only a moderate basal SF ( $\sim 0.3$ – $0.4$ ). The point X has a low SF ( $\sim 0.11$ ) while the neighboring point Y has a high SF ( $\sim 0.49$ ). This high mismatch in SF causes load shedding from grain at point Y onto the grain at point X. These observations are consistent with the results of simulations in [11–14,24], where a high stress concentration is induced in the hard oriented grain due to time

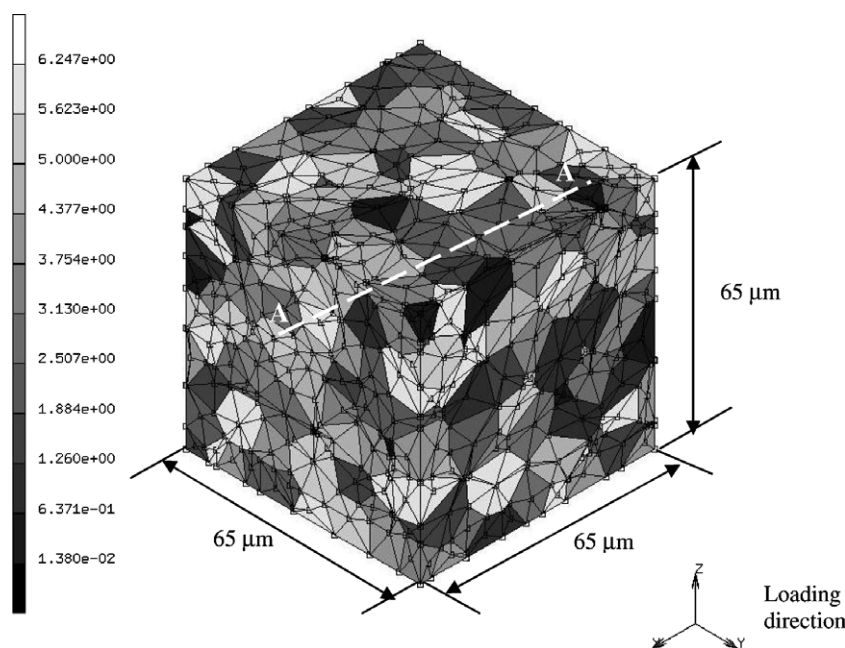


Fig. 6. FE model for polycrystalline Ti-6242, which is statistically equivalent to the OIM scan of the critical region of microstructure MS1. Also shown is the contour of 'c'-axis orientation distribution (radians).

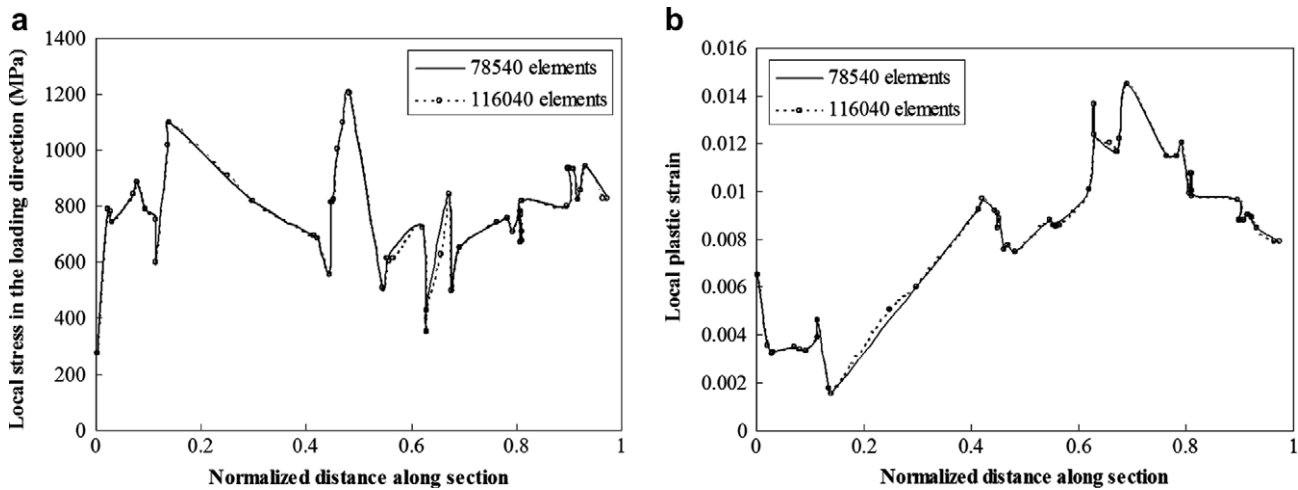


Fig. 7. Distribution of local variables: (a) loading direction stress ( $\sigma_{22}$ ) and (b) local plastic strain along a section parallel to the  $x$ -axis at the end of 1000 s for a creep simulation on the two models of microstructure MS1 with two different mesh densities.

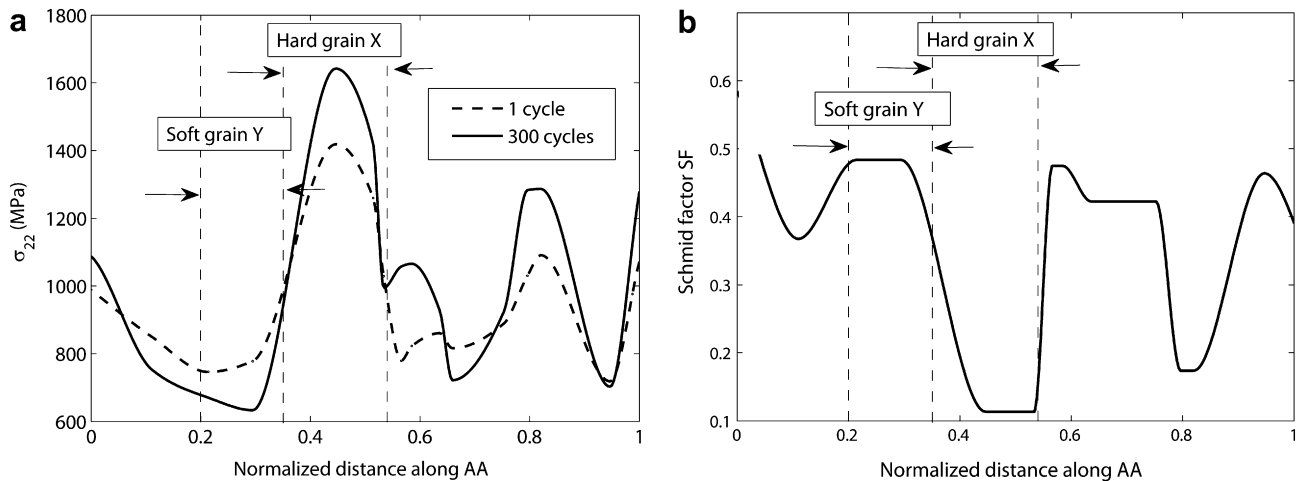


Fig. 8. Distribution of local variables: (a) loading direction stress ( $\sigma_{22}$ ), (b) prominent prismatic Schmid factor along a section AA parallel to the  $x$ -axis at the end of 1 and 300 dwell cycles for a dwell fatigue simulation of the critical FE MS1 model.

dependent plastic strain accumulation in the neighboring soft oriented grain. This analysis demonstrates the importance of load shedding induced stress concentrations in a hard grain on the development of a criterion for crack initiation at the level of a grain.

### 3. Crack nucleation criterion based on local variables in fem solution

The term nucleation has been used in the literature to depict different phenomena and the main difference arises from the length scale under consideration [1]. The present work proposes criterion for grain-level crack nucleation at the length scale of individual grains. The criterion is proposed in terms of variables that are calculated using the crystal plasticity based computational model at the slip system level. However, the proposed criterion does take into account dislocation distributions that occur due to the impedance in their transfer from soft grains to hard grains.

#### 3.1. A few relevant models of crack nucleation in the literature

Crack nucleation in metallic grains has been modeled analytically by a few researchers using dislocation theory. The crack initi-

ation mechanism using a dislocation pile up model at the grain boundary of a crystalline solid has been explained by Stroh [25]. Assuming that the local stress concentration at the tip of the dislocation pile up is directly proportional to the number of dislocations, the model proposes that a crack initiates if:

$$n\sigma_n \geq 12\alpha G \tag{1}$$

where  $n$  is the number of dislocations in the pile up,  $\sigma_n$  is the stress normal to the slip plane,  $G$  is the shear modulus and  $\alpha = \frac{\gamma}{bG}$  is a material constant in which  $\gamma$  is the surface energy and  $b$  is the Burgers vector. Only mode I crack initiation is considered in this normal stress based model. Consideration of only the normal stresses has been questioned in [26]. It was shown that for zinc single crystals, the stress normal to the cleavage plane had different values at fracture for different crystal orientations. While it was concluded that the normal component of stress is not the only factor that caused fracture, no alternative was proposed. In Ref. [8], for the dwell fatigue of Ti alloys it is proposed that an optimum combination of the shear stress and the tensile normal stress leads to crack nucleation in the hard grain. Crack nucleation by dislocation pileups was also studied in detail in [20,27]. In [20], it was proposed that a dislocation pile up leads to a mode II crack by dislocation coalescence. Dis-

location pileup in this model is represented from equilibrium consideration in a grain of size  $d$ , yielding a cleavage fracture criterion in [27] as

$$\sigma_E \geq \left( \frac{2\gamma G}{\pi(1-\nu)d} \right)^{1/2} \quad (2)$$

The stress  $\sigma_E$  required to fracture a grain is inversely related to the square root of the grain size. While the models may have differences, there is concurrence on one idea: that the crack nucleates in the hard grain as a consequence of stress concentration caused by a dislocation pileup in a neighboring soft grain.

Various fatigue failure models have explored the equivalence between continuous dislocation pileups and cracks [28]. In [29], a dislocation model has been developed for fatigue failure due to dislocation dipoles. A factor to predict micro-crack nucleation at grain boundaries due to accumulation of deformation twins in  $\gamma$ -Ti-Al alloy has been proposed in [30]. An inverse square root relation between the local fracture stress and the length of the dislocation pile up is shown in [31], similar to the relation between the local fracture stress and the length of a pre-existing crack [32]. Similarities in the stress field ahead of a dislocation pileup and a crack have been discussed in [20,33–35]. Based on these arguments, equivalence in the functional forms is exploited to develop a grain-level crack nucleation criterion.

### 3.2. A critical stress criterion based on slip system stress fields

A crack nucleation criterion is first postulated with the understanding that a brittle crack is nucleated in the hard grain due to stress concentration caused by dislocation pileup in the neighboring soft grain. In this criterion, micro-cracking is triggered by an effective stress, in terms of the slip system normal and tangential stress components, reaching a critical value. The stress component normal to a slip plane is  $T_n = n_i^b (\sigma_{ij} n_j^b)$ , where  $\sigma_{ij}$  is the Cauchy stress tensor and  $n_i^b$  corresponds to components of the unit outward normal to the slip plane. Only the tensile normal stress  $\langle T_n \rangle$  is considered, because a compressive normal stress will not contribute to opening a crack. Here  $\langle \rangle$  is the McCauley bracket. The shear traction component  $T_t$  is obtained from the vector subtraction of  $T_n$  from the traction vector on the plane, i.e.  $T_t t^b = T - T_n n^b$  where  $t^b$  is the unit vector tangent to the plane. An effective resultant traction  $T_{\text{eff}}$  is defined in [36], in terms of the normal and shear stresses for mixed-mode fracture, as

$$T_{\text{eff}} = \sqrt{\langle T_n \rangle^2 + \beta T_t^2} \quad (3)$$

Here,  $\beta$  is a shear stress factor, which is used to assign different weights to the normal and shear traction components for mixed-mode cohesive laws, as discussed in [37]. It is approximately defined as the ratio of the shear to normal fracture toughness of the material, i.e.  $\beta \approx \frac{K_{IIc}}{K_{IC}}$ . For Ti-64,  $\beta$  has been evaluated to be 0.7071 in [38], which is used in the present work. Sensitivity studies with different  $\beta$ 's have shown that for  $\langle c+a \rangle$  oriented hard grains, the value of  $T_{\text{eff}}$  is not sensitive to  $\beta$ , due to the large magnitude of  $T_n$ . A critical stress crack nucleation criterion is thus proposed as

$$T_{\text{eff}} = \sqrt{\langle T_n \rangle^2 + \beta T_t^2} \geq T_{\text{cr}} \quad (4)$$

where  $T_{\text{cr}}$  is a material dependent critical stress value.

#### 3.2.1. Test of the effective stress based criterion

Validation of the crack initiation criterion proposed in Eq. (4) necessitates determining a critical stress  $T_{\text{cr}}$  that will be valid for all regions of observed cracking. Results of crystal plasticity FEM simulations for dwell loading conditions for the critical regions in the micrograph are used for this purpose. While complete failure occurs in the MS1 sample at 352 cycles, the growth pattern has

**Table 2**

Important microstructural variables in five grains with highest values of  $T_{\text{eff}}$  from FE simulations under dwell loading, at the end of 300 cycles. The model is for the critical region in the sample MS1

Grain no	$T_{\text{eff}}$ (MPa)	$\theta_c$ (°)	Prism SF	Basal SF
1	1719.44	29.39	0.1134	0.4260
2	1609.23	32.34	0.1377	0.4164
3	1531.38	16.28	0.0393	0.2617
4	1520.48	28.36	0.1126	0.3995
5	1443.19	10.50	0.0160	0.1780

not been recorded ultrasonically. From observations made for the MS2 and MS3 samples, two probable crack initiation times are considered, viz. (i) 80% of complete failure i.e. 282 cycles, or (ii) 85% of complete failure i.e. 300 cycles. Correspondingly, the crack nucleation criterion in Eq. (4) is expected to be met in the critical FE model at the same number of cycles. Results of the computational model are analyzed at the end of 282 and 300 dwell cycles respectively with respect to the location and time of crack initiation. These are discussed next.

- (a) *Location of crack initiation:* At the end of 282 and 300 cycles,  $T_{\text{eff}}$  in Eq. (4) is calculated on each slip plane at each integration point of every element in the grains. The five grains with the highest values of  $T_{\text{eff}}$  at element integration points are subsequently analyzed. The same five grains are found to have the maximum value of  $T_{\text{eff}}$  for both the loading times. The highest values of  $T_{\text{eff}}$  are found on the basal plane, when compared with all the other slip planes. This result agrees with the experimental observation of near basal orientation of the fracture facets. Table 2 delineates the microstructural features of these top five grains; viz. the 'c'-axis orientation, prismatic SF and basal SF. Each of these grains has a 'c'-axis orientation in the range 0–30°, a prismatic SF in the range 0–0.15 and a basal SF in the range 0.3–0.45. This is in good agreement with the observed features of the failure sites in [22], as discussed in Section 2.1.1. The agreement with experiments qualitatively validates the predictive capability of the criterion, in terms of the location of crack initiation.
- (b) *Number of cycles to crack initiation:* The grain labeled X in Fig. 8a has the highest value of  $T_{\text{eff}}$  in comparison with all other grains. The corresponding SF is shown in Fig. 8b. The maximum value at 282 cycles is  $T_{\text{eff}}^{\text{max}} = 1718$  MPa; while at 300 cycles it is  $T_{\text{eff}}^{\text{max}} = 1720$  MPa, an increase by only 0.1%. The evolution of  $T_{\text{eff}}^{\text{max}}$  with number of cycles is depicted in Fig. 9. Although  $T_{\text{eff}}^{\text{max}}$  monotonically increases with dwell cycles, the rate of change per cycle is very low at higher cycles (increases only by 3.7% in the last 250 cycles). A similar trend of evolution of local stress components has been reported in [12,13]. Since the right hand side of Eq. (4), i.e.  $T_{\text{cr}}$  is a constant, this means that even a small variation in  $T_{\text{cr}}$  might cause the predicted dwell fatigue life to vary by hundreds of cycles. For example, a 3.5% change in  $T_{\text{cr}}$  from 1660 MPa to 1724 MPa will result in a 150% change in the predicted life from 100 cycles to 352 cycles. Consequently, an amendment of the right hand side of the critical stress based criterion is pursued, taking into account other evolving variables in the analysis.

### 3.3. Crack Nucleation Criterion Accounting for Dislocation Pileup

As discussed in Section 3.1, the equivalence between crack formation ahead of a crack and dislocation pileups, forms the basis of the modification of criterion (4). The proposed framework builds

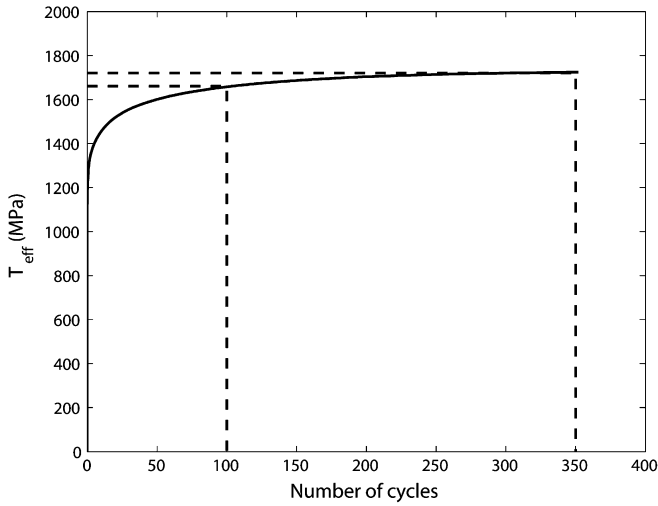


Fig. 9. Evolution of  $T_{\text{eff}}$  with number of cycles, for grain at point X in the dwell fatigue simulation of the critical MS1 FE model.

upon the fracture criterion proposed by Griffith [39] using the stress analysis of Irwin [40]. From the condition that catastrophic fracture can occur when strain energy release rate is sufficient to overcome the rate of surface energy needed for breaking of bonds as well as energy dissipation due to plastic flow, the criterion has been proposed as

$$\sqrt{\sigma^2 + \beta\tau^2} \geq \alpha_1 \sqrt{\frac{G_c}{a_0}} \quad (5)$$

Here  $a_0$  is the pre-existing crack length,  $G_c$  is the critical strain energy release rate and  $\alpha_1$  is a material dependent parameter.  $\sigma$  is the normal stress and  $\tau$  is the shear stress acting on the plane of the crack. A similar criterion [36] may also be derived from the stress intensity approach, in which the material is assumed to withstand crack tip stresses up to a critical value of the stress intensity factor  $K_{Ic}$ , stated as

$$\sqrt{\sigma^2 + \beta\tau^2} \geq \alpha_2 \frac{K_{Ic}}{\sqrt{a_0}} \quad (6)$$

where  $\alpha_2$  is a geometry dependent parameter.

The crack initiation criterion due to load shedding in the hard grain is developed in a similar vein. Dislocations pile up near the boundary of a soft grain due to orientation mismatch with the adjoining hard grains. The dislocation pileup acts in a similar way as a crack that scales with the length of the pileup. Correspondingly, the right hand side of Eq. (4) is modified to have an inverse square root dependence on the pile up length  $d$ , resulting in the crack nucleation criterion:

$$T_{\text{eff}} = \sqrt{(T_n)^2 + \beta T_t^2} \geq \frac{R_c}{\sqrt{d}} \quad \text{or equivalently} \quad (7a)$$

$$R = T_{\text{eff}} \cdot \sqrt{d} \geq R_c \quad (7b)$$

where  $R_c$  is a parameter that depends on the material elastic properties, as well as the critical strain energy release rate  $G_c$ .  $R_c$  has units of the stress intensity factor i.e.  $\text{MPa}\sqrt{\mu\text{m}}$ . As more dislocations are added to the pile up with time, the pile up length  $d$  in the soft grain increases requiring a smaller  $T_{\text{eff}}$  to initiate a crack. The crystal plasticity FEM model developed in [11–14] does not explicitly consider dislocation density as an output variable. Hence an approximate method of estimating pile up length  $d$  from the results of the crystal plasticity FE simulations is described next.

### 3.3.1. Estimating the dislocation pileup length 'd' in the neighboring grain

A continuous distribution function of the dislocation density (per unit length)  $\rho(x)$  has been derived as a function of the distance  $x$  from the dislocation barrier in [41,42] as

$$\rho^l(x) = \frac{2\tau}{Gb} \sqrt{\frac{d-x}{x}} \Rightarrow d = \left( \frac{[\rho^l(x)]^2 G^2 b^2}{4\tau^2} + 1 \right) x \quad (8)$$

where  $d$  is the pileup length,  $G$  is the shear modulus,  $\tau$  is the shear stress and  $b$  is the magnitude of the Burgers vector. If the dislocation density is known at a specific location  $x$ , the pile up length may be solved from Eq. (8). In the crystal plasticity FEM analysis, where  $\rho^l(x)$  is not an explicit variable, it can be derived from known output variables in the post-processing phase.

The total dislocation density is assumed to be the sum of the density of statistically stored dislocations (SSDs) and the density of geometrically necessary dislocations (GNDs). The SSD density per unit area, corresponding to homogenous plastic deformation, and the GND density per unit area that accommodates plastic strain gradients, have been expressed in [21] as

$$\rho_{\text{SSD}}^A = \frac{\sqrt{3}\bar{\epsilon}^p}{b\ell^*} \quad \text{and} \quad \rho_{\text{GND}}^A = \frac{\eta^p}{b} \quad (9)$$

where  $\ell^*$  denotes the material length scale which is of the order of  $(\frac{G}{\sigma_{\text{yield}}})^2 b$  from [43]. In this work,  $\ell^*$  is taken to be  $5 \mu\text{m}$  from [44]. The equivalent plastic strain and a measure of the effective plastic strain gradient are defined in terms of the plastic part of the deformation gradient tensor  $F^p$ , which is available from the FEM output data, as

$$\begin{aligned} \bar{\epsilon}^p &= \left( \frac{2}{3} \left\{ \frac{1}{2} (F^{pT} F^p - I) \right\}^T \left\{ \frac{1}{2} (F^{pT} F^p - I) \right\} \right)^{\frac{1}{2}}, \quad \eta^p \\ &= \left( \frac{1}{\det F^p} F^p \cdot (\nabla \times F^p) : \frac{1}{\det F^p} F^p \cdot (\nabla \times F^p) \right)^{\frac{1}{2}} \end{aligned} \quad (10)$$

The curl of the plastic deformation gradient, expressed as  $\nabla \times F^p = \epsilon_{irs} \frac{\partial F_{js}^p}{\partial x_r}$  with  $\epsilon_{irs}$  being the permutation symbol, is a third order tensor with 27 components. The curl of the plastic deformation gradient, expressed as  $\nabla \times F^p = \epsilon_{irs} \frac{\partial F_{js}^p}{\partial x_r}$  with  $\epsilon_{irs}$  being the permutation symbol, is a third order tensor with 27 components. Numerically, each component of  $\frac{\partial F_{ij}^p}{\partial x_r}$  may be calculated using a weighted difference formula involving surrounding points as

$$\frac{\partial F_{ij}^p}{\partial x_r} = \frac{\sum_{m=1}^n \frac{1}{r_m} \left( \frac{F_{ij}^p|_k - (F_{ij}^p|_m)}{(x_r|_k - (x_r|_m))} \right)}{\sum_{m=1}^n \frac{1}{r_m}} \quad (11)$$

where 'n' is the number of points that lie within a sphere of assumed radius ( $5 \mu\text{m}$ ) from the 'kth' point at which  $\frac{\partial F_{ij}^p}{\partial x_r}$  is being evaluated. The weighting function is taken as the inverse of  $r_m$ , which is the distance between the 'kth' point and the surrounding 'mth' point.

Since,  $F^p$  is a state variable in the crystal plasticity simulations,  $\bar{\epsilon}^p$  and  $\eta^p$  in Eq. (9) can be determined at integration points and consequently the total dislocation density per unit area  $\rho^A(x)$  can be determined as

$$\rho^A(x) = \rho_{\text{SSD}}^A(x) + \rho_{\text{GND}}^A \quad (12)$$

The dislocation density distribution function per unit length  $\rho^l(x)$  is based of single slip activity while the total dislocation density per unit area  $\rho^A(x)$  is a cumulative effect of slip on multiple slip systems. It is assumed that the dislocation pileup for  $\rho^A(x)$  follows the same distribution function as for single slip  $\rho^l(x)$  in Eq. (8). The dislocation density per unit length  $\rho^l(x)$  in Eq. (8) is obtained from  $\rho^A(x)$  by multiplying with the dislocation line length. For <a> type

slip in Ti-6242 the dislocation line length is found to be 250 nm in [15]. Since the dislocation density may be the result of slip on multiple planes, no one plane is chosen for calculating  $x$  towards evaluating the pileup length  $d$  in Eq. (8). In consistency with the effective dislocation density measure,  $x$  is taken as the distance of the integration point to the nearest grain boundary. The pileup length  $d$  is restated as

$$d = [(A_1 \varepsilon^p + A_2 \eta^p)^2 + 1]x \quad \text{where } A_1 = \frac{\sqrt{3}G}{2\tau l^*}, A_2 = \frac{G}{2\tau} \quad (13)$$

In the FE model, each grain is meshed with several elements and hence each grain boundary is shared by a number of elements. Thus, an effective dislocation pileup length  $\bar{d}$  for a given grain boundary is computed as the weighted average of pileup lengths  $d_i$  corresponding to multiple integration points in the soft grain adjacent to a hard grain, i.e.

$$\bar{d} = \frac{\sum_{i=1}^p W(r_i) d_i}{\sum_{i=1}^p W(r_i)} \quad (14)$$

where,  $p$  is the number of integration points in consideration,  $r_i$  is the distance between the point at which the criterion is being evaluated and the element integration point  $i$  in the soft grain and the weighting function is given in [45] as  $W(r) = \frac{1}{(2\pi)^{3/2} l^3} \exp(-\frac{r^2}{2l^2})$ , which tends to zero beyond a certain distance. The parameter  $l$  determines the size of the region that contributes to  $\bar{d}$ . A numerical sensitivity analysis is conducted to evaluate the effect of different values of  $l$  on the value of  $R$  at different locations. It is inferred that the value of  $R$  does not vary much for  $l \geq 5\mu\text{m}$ , which is its chosen value.

Finally, substituting Eq. (13) and Eq. (14) in Eq. (7), yields the modified grain-level crack nucleation criterion as

$$T_{\text{eff}} = \sqrt{\langle T_n \rangle^2 + \beta T_t^2} \geq \frac{R_c}{\sqrt{\frac{\sum_{i=1}^p W(r_i) [(A_1 \varepsilon_i^p + A_2 \eta_i^p)^2 + 1] x_i}{\sum_{i=1}^p W(r_i)}}} \quad (15a)$$

or equivalently

$$R = T_{\text{eff}} \cdot \sqrt{\frac{\sum_{i=1}^p W(r_i) [(A_1 \varepsilon_i^p + A_2 \eta_i^p)^2 + 1] x_i}{\sum_{i=1}^p W(r_i)}} \geq R_c \quad (15b)$$

The left hand side of Eq. (15a) evaluates  $T_{\text{eff}}$  at a point in one (hard) grain, while the right hand side incorporates the plastic strain  $\varepsilon^p$  and its gradient  $\eta^p$  in an adjacent softer grain. The variable  $R$  is checked for every element integration point near the grain boundary in the crystal plasticity FE model in the post-processing stage. Various parameters used in Eq. (15) are listed in Table 3. The condition posed in Eq. (15) is non-local in that the stress required to initiate a crack at a point in the hard grain depends on the plastic strain and gradient of plastic strain in the neighboring soft grain.

**Table 3**  
Parameters used in the crack nucleation criterion of Eq. Eq. (15)

Material parameter	Value
Shear modulus $G$	48 GPa
Magnitude of Burger's vector $b$	0.30 nm
Material length scale $l$	5 $\mu\text{m}$
Non-local length parameter $l$	5 $\mu\text{m}$

#### 4. Calibration and validations of the nucleation criterion

##### 4.1. Calibration of $R_c$

The material parameter  $R_c$  in the right hand side of Eq. (15a) is calibrated from the results of FE simulations of the sample microstructure MS1 at the critical region containing the crack, under 2-min dwell loading conditions. The development of the statistically equivalent FE models has been discussed in Section 2.2.2. The total life of this sample is recorded as 352 cycles by acoustic microscopy. Based on the observations made for the samples MS2 and MS3 in Section 2.1.2, initiation is assumed at two alternate percentages of the total life, viz. 80% and 85% (i.e. 282 and 300 cycles). To evaluate  $R_c$  corresponding to the two percentages, the variable  $R$  in Eq. (15b) is determined at integration points that are closest to each grain boundary for all grains at the end of 282 and 300 cycles. The hard grain of the grain pair with maximum value of  $R$  is located. The same grain, labeled X in Fig. 8a has the highest  $R$  for both the times. Fig. 10a shows the continuous evolution of this maximum  $R$  with the number of cycles. From Eq. (15b), the value of  $R$  may be equated to  $R_c$  at initiation. For the two scenarios, the

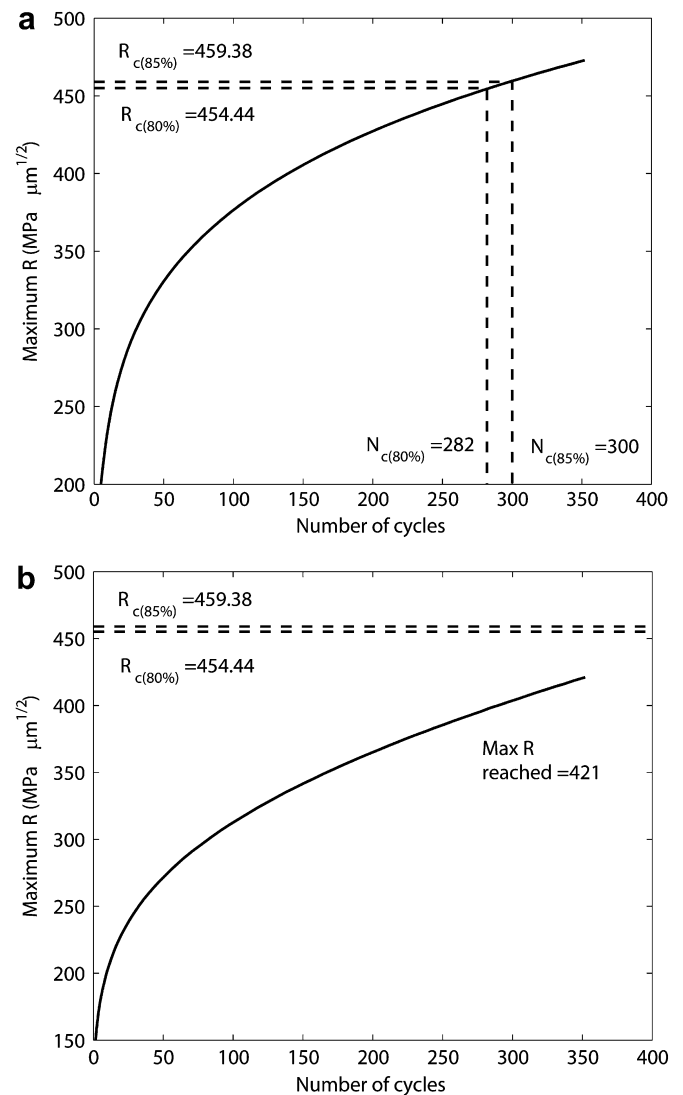


**Fig. 10.** Evolution of the local maximum  $R$  over number of cycles at a maximum load of 869 MPa with 2-min hold time for: (a) critical FE model, (b) non-critical FE model.

threshold values are determined to be  $R_{c(80)} = 454.44 \text{ MPa } \mu(m)^{\frac{1}{2}}$  and  $R_{c(85\%)} = 459.38 \text{ MPa } \mu(m)^{\frac{1}{2}}$  corresponding to 282 cycles and 300 cycles respectively. Other statistically equivalent realizations of the FE model also yield threshold values that are within 1% of the above values. Hence these are used for predicting crack initiation in subsequent experiments.

4.2. Validation of the nucleation model

4.2.1. Predictions and analysis with sample MS1 at critical and non-critical regions

The critical and non-critical regions of a local polycrystalline microstructure are classified as those with and without dwell fatigue cracks, as observed in the ultrasonic analyses. Statistically representative FE models of the OIM scanned images are generated for these regions following the procedure described in Section 2.2.2. It has been observed in the previous experimental and analytical studies that hard grains surrounded by large micro-textured regions of soft grains are prime candidates for load shedding induced micro cracking. Consequently, microstructural characteristics of the FE models at the critical and non-critical regions representing this feature are analyzed and plotted in Fig. 11. Grains that have low  $c$ -axis orientation  $\theta_c$ , a low prism SF and a low to moderate basal SF are classified as “hard”, while grains with a basal or prism SF higher than 0.48 are classified as “soft”. The figures are histograms of the distribution of the volume fraction of soft grains in the neighborhood of every hard grain in the two microstructures. Fig. 11a shows that the critical model has two hard grains with 70% soft surrounding, three hard grains each with 50% and 60% soft surrounding while all other hard grains with less than 50% soft sur-

rounding. In contrast, Fig. 11b shows that the non-critical model has no hard grain with more than 50% soft surrounding. These statistics indicate that the critical model has more locations that are more prone to occurrence of load shedding as compared to the non-critical model.

FE simulation of the non-critical microstructural model is conducted under 2-min. dwell loading conditions and the value of  $R$  is evaluated near all grain boundaries throughout the simulation. Fig. 10b plots the evolution of the maximum  $R$  vs. the cycles. The maximum  $R$  reached at the end of 352 cycles is only  $421 \text{ MPa } \sqrt{\mu\text{m}}$ , which is less than both the threshold values of  $R_c$ . Consequently, the criterion does not predict a crack initiation in this non-critical model, which matches the experimental observation. Thus, if a model has higher number of hard-soft grain combinations, then the criterion will predict a lower life.

4.2.2. Predictions and analysis with samples MS2 and MS3 at critical regions

For the MS2 microstructure at a critical region, the FE model is generated to be statistically equivalent to an OIM scan surrounding

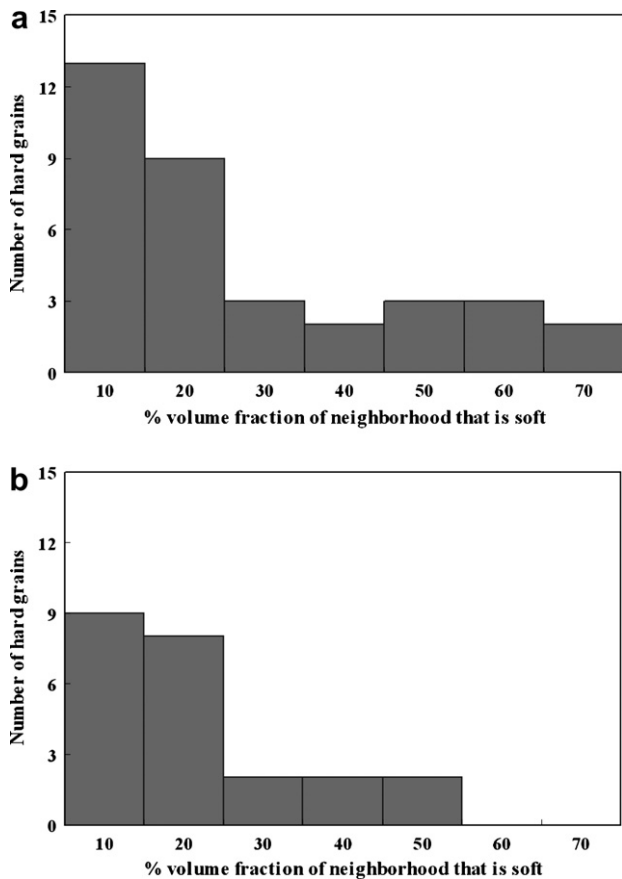


Fig. 11. Distributions of hard grains and fraction of soft neighborhood for (a) critical FE model, (b) non-critical FE model.

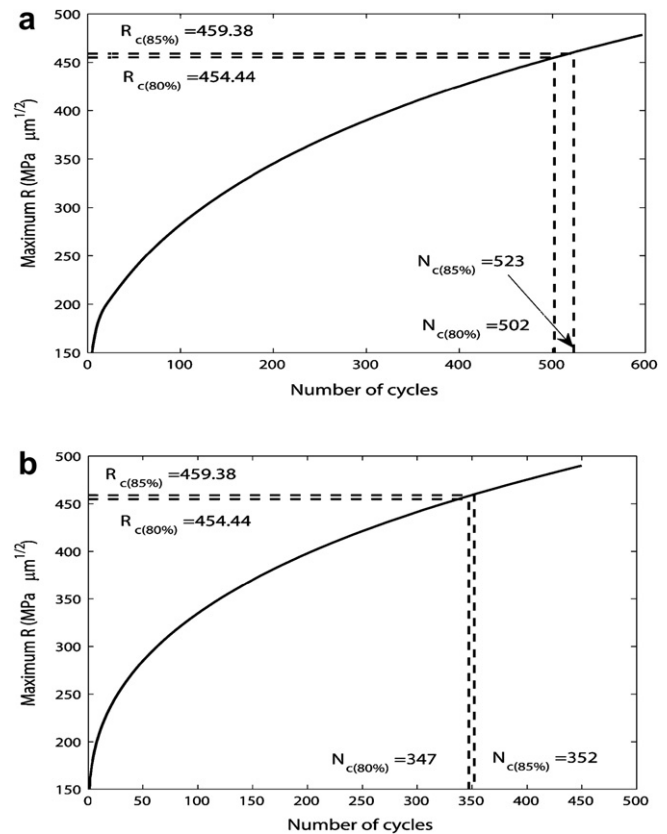


Fig. 12. Evolution of the maximum  $R$  over number of cycles for the FE models of microstructures (a) MS2, (b) MS3.

Table 4

Comparison of predicted cycles to crack initiation with experimentally observed life

Microstructure label	Time to crack initiation (experiment)	Time to crack initiation (predicted)		% Relative error	
		Calibrated at 80% life	Calibrated at 85% life	Calibrated at 80% life	Calibrated at 85% life
MS2	530 cycles	502 cycles	523 cycles	5.28	1.32
MS3	380 cycles	347 cycles	352 cycles	8.68	7.37

a secondary crack, for which the crack initiation time is shown in Fig. 2 as 530 cycles. The simulation under dwell loading with modulation is performed for 663 cycles. Fig. 12a shows the evolution of

the maximum  $R$  with cycles. The number of cycles to initiation  $N_{c(80)}$  and  $N_{c(85)}$  are evaluated from where the curve meets the threshold values  $R_{c(80)}$  and  $R_{c(85)}$ . The cycles to initiation are found

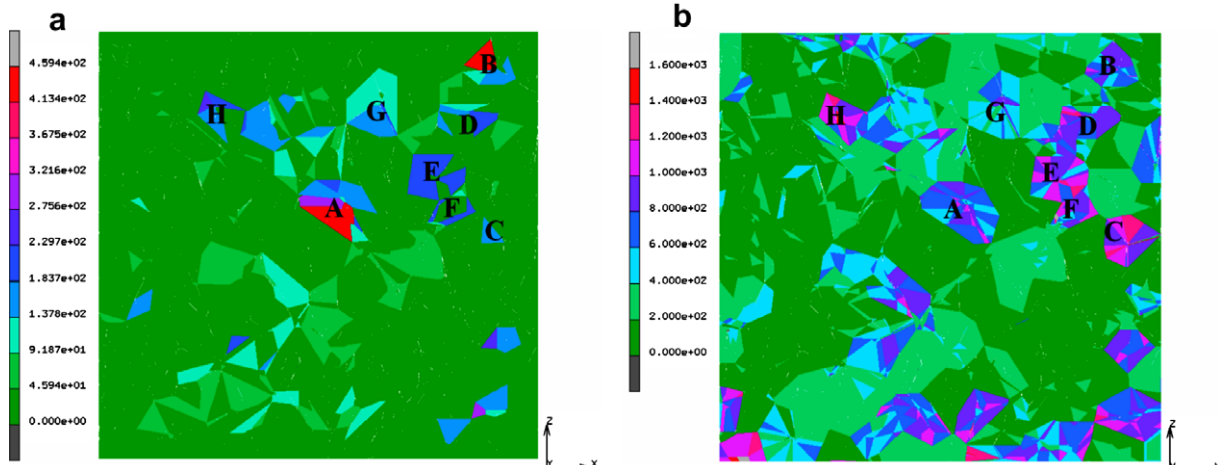


Fig. 13. Contour plots showing the distribution of (a)  $R$ , and (b)  $T_{eff}$  across a cross section AA perpendicular to the loading direction, for the critical FE model of microstructure MS1 at the end of 300 dwell cycles.

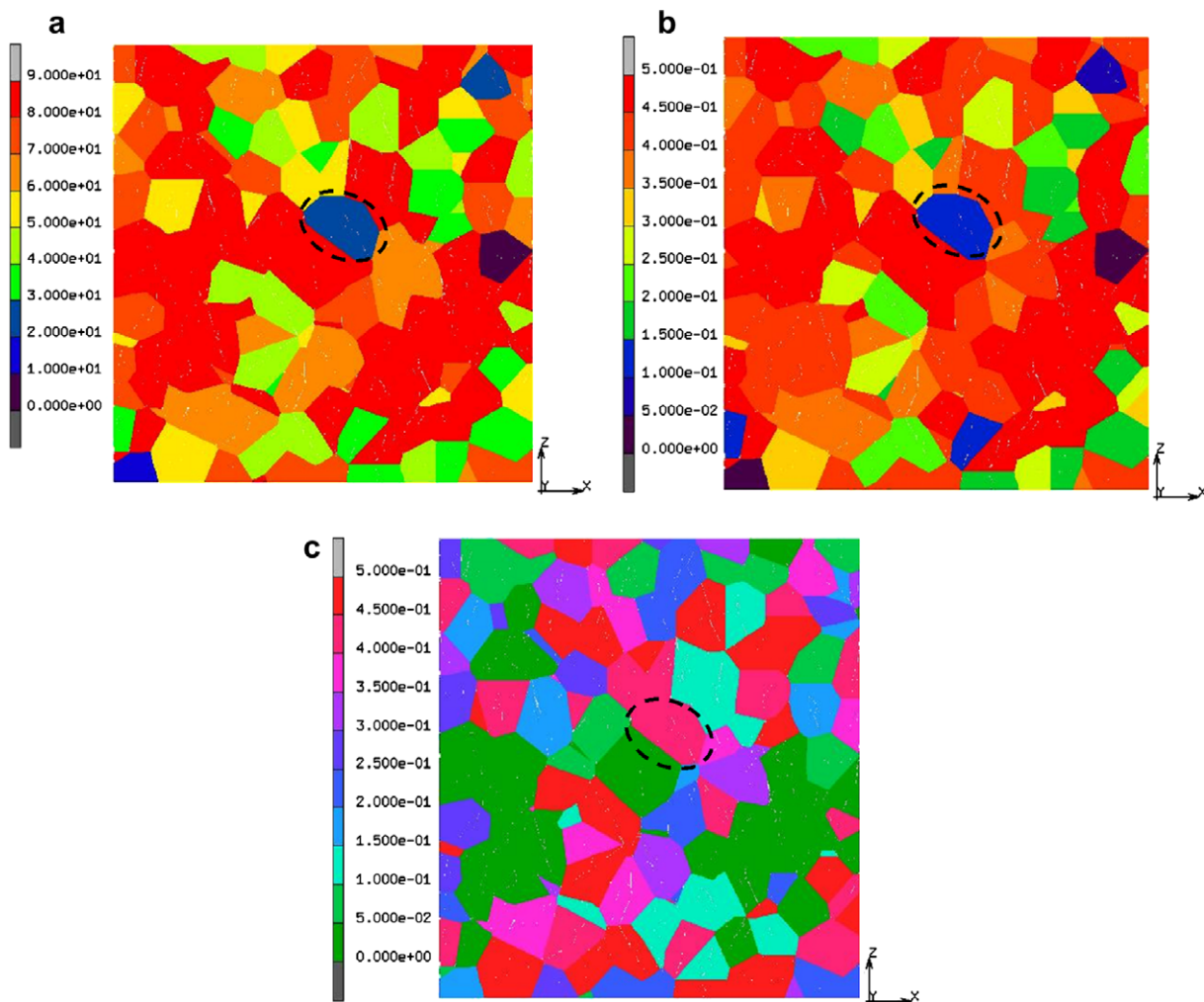


Fig. 14. Contour plots showing the distribution of (a) 'c'-axis orientation (degrees), (b) prism  $SF$  and (c) basal  $SF$ , across a cross section of the critical FE model of microstructure MS1.

to be  $N_{c(80)} = 502$  and  $N_{c(85)} = 523$ . The difference with the experimental value from Fig. 2 is 5.28% for 80% of life and only 1.32% for 85% of life. This agreement is considered to be excellent.

Again, for the MS3 microstructure at a critical region, the FE model is generated using statistics of the OIM scans at a failure site. The 2-min. dwell fatigue simulation is performed for 447 cycles and the corresponding evolution of maximum  $R$  is plotted in Fig. 12b. The cycles to initiation are found to be  $N_{c(80)} = 347$  and  $N_{c(85)} = 352$ .

This corresponds to a 8.68% relative error with respect to experimental value for 80% life and a 7.37% relative error for 85% life. Results of predictions by the crack nucleation criterion are summarized in the Table 4. In general, the calibrated value of  $R_c$  at 85% life is seen to work better than at 80% life.

#### 4.2.3. Prediction of the crack initiation location

As a final validation study, the predicted location of crack initiation in MS1 is examined. Microstructural features of regions that have high values of  $R$  are investigated. Fig. 13 shows contour plots of  $R$  and  $T_{eff}$  respectively across a cross section A–A of the critical FE model perpendicular to the loading direction ( $y$ -direction) at 300 cycles. The section passes through the grain A, which has the maximum value of  $R$ . The labeled grains A–H too show moderate to high stress concentrations and values of  $R$  and may be considered as potential crack initiation sites. Contour plots of the  $c$ -axis orientation, prismatic  $SF$  and basal  $SF$  across the cross section are shown in Fig. 14. The largest of the three values of the basal and prismatic  $SF$ 's are shown in these plots similar to [22]. The grain A, shown with a dotted ellipse in each figure, has a ' $c$ '-axis orientation of  $29^\circ$ , a prismatic  $SF$  of 0.11 and a basal  $SF$  of 0.42. These values agree well with the observed features of dwell fatigue failure sites in [22]. Table 5 shows a range of the microstructural features for grains A–H. While the microstructural features of grains A, B and C match the experimentally observed features, they deviate for the other grains. Furthermore, grain A with the largest  $R$  has a very large neighboring soft grain with  $\sim 0.5$  prism  $SF$  (situated to the lower left of grain A in Fig. 14b). This is the grain that shows up as grain Y in the plot shown in Fig. 8b. Examining cross-sections above and below A–A have shown that both above and below grain A, there is a large chunk of grains with a high prism activity, which is not the case for grains B and C. Thus, grain A has a larger fraction of its neighborhood that is soft, and hence it is only likely that it be the most critical grain. Table 6 summarizes the microstructural features of the grains that satisfy the criterion in MS2 and MS3.

**Table 5**  
Microstructural features of key grains in the FE model of microstructure MS1 at critical region

Grain	$\theta_c$ ( $^\circ$ )	Prism $SF$	Basal $SF$
A	20–30	0.1–0.15	0.4–0.45
B	20–30	0.05–0.1	0.35–0.4
C	0–10	0–0.05	0.05–0.1
D	30–40	0.15–0.2	0.45–0.5
E	30–40	0.2–0.25	0.35–0.4
F	30–40	0.2–0.25	0.45–0.5
G	40–50	0.25–0.3	0.4–0.45
H	30–40	0.15–0.2	0.45–0.5

**Table 6**  
Microstructural features of predicted location of crack initiation in dwell fatigue of Ti-6242

Microstructure label	$\theta_c$ ( $^\circ$ )	SF prism	SF basal
MS1	29.39	0.1134	0.426
MS2	17.86	0.0047	0.2832
MS3	32.05	0.133	0.447

In each case, crack initiation is predicted for a grain with low ' $c$ '-axis orientation ( $0$ – $30^\circ$ ), low prism activity ( $0$ – $0.1$ ) and low to moderate basal activity ( $0.3$ – $0.45$ ). These results prove convincingly the predictive capability of the proposed criterion.

## 5. Conclusions

This paper presents the development of a grain-level crack nucleation criterion in polycrystalline Ti-6242 alloy. The criterion is calibrated and validated with extensive experimental observations ranging from ultrasonic techniques like acoustic microscopy to orientation imaging microscopy (OIM) and fractography. A major tool used for the development of the nucleation model is an experimentally validated, rate and size dependent, crystal plasticity model that is used for the computational modeling of the mechanical response at the level of individual grains. Furthermore, the 3D FE model is constructed to have morphological and crystallographic characteristics that are statistically equivalent to those observed in an OIM scan of the Ti-6242 alloy. Specific characteristics include orientation, misorientation and micro-texture distribution, as well as distributions of grain volume and near neighbor distances. The model motivates that load shedding between grains is a prime cause of early crack initiation in Ti-6242.

Comparison with experiments demonstrates that a critical stress based criterion is unable to capture the true effect of load shedding, especially that of straining of soft grains adjacent to a hard grain. Consequently, a non-local criterion that depends on local effective stresses in the hard grain, as well as the non-local plastic strains and strain gradients in adjacent grains, is developed from considerations that dwell fatigue crack initiates due to stress concentration caused by a dislocation pile up at the boundary of hard and soft grains. The functional form is motivated by the similarity between crack initiation ahead of an existing crack and a dislocation pile up. Consequently, the crack length in this model is replaced by the dislocation pileup length. A slip system level effective stress, defined in terms of the normal and shear stresses on the slip planes, is an important parameter in nucleation model. The local stress required for crack initiation has an inverse square root dependence on the dislocation pileup length. To utilize the output variables of the crystal plasticity simulations in the nucleation model, the length of the dislocation pileup is expressed as a function of the effective plastic strain and the effective gradient of plastic strain.

Experimental results from ultrasonic monitoring are used to calibrate the nucleation criterion that is based on local variables in the FE model from the dwell fatigue simulation. Critical microstructural features at a failure site of the Ti-6242 specimen failed are retained in the statistically equivalent FE model. Once calibrated, the criterion is successfully validated through accurate predictions of the number of cycles to failure as well as the critical features of the failure site in other dwell fatigue experiments. Important microstructural parameters have been identified from sensitivity studies viz. the  $c$ -axis orientation, and the  $SF$ 's of the basal and prismatic slip systems. The proposed criterion is sensitive to critical microstructural conditions. Both simulations and experiments points to the fact that a hard grain surrounded by a large volume fraction of soft grains is a prime candidate for dwell fatigue crack nucleation.

In conclusion, this paper successfully develops an experimentally validated, microstructure sensitive, slip system level dwell fatigue crack nucleation criterion for Ti-6242. While the criterion is believed to perform well as long as the identified mechanisms of fatigue crack nucleation remain the same, additional features like defects in the microstructure may make the model more realistic and could be a subject of future study.

## Acknowledgements

The authors are grateful to Professors Jim Williams, Mike Mills, Stan Rokhlin and Drs M. Groeber, A. Bhattacharjee and B. Zoofan for providing guidance and experimental data. This work has been supported by the Federal Aviation Administration through grant No. DTFA03-01-C-0019 (Program Director: Dr. Joe Wilson). This support is gratefully acknowledged. The authors acknowledge the insightful suggestions of Drs. A. Woodfield, B. Kalb, A. Chatterjee, J. Hall, J. Schirra, D. Nissley, A. Walker and R. Corran on various aspects of this work. Computer support by the Ohio Supercomputer Center through grant # PAS813-2 is also acknowledged.

## References

- [1] Suresh S. *Fatigue of materials*. Cambridge: Cambridge University Press; 1991.
- [2] Woodfield AP, Gorman MD, Corderman RR, Sutliff JA, Yamrom B. Effect of microstructure on dwell fatigue behaviour of Ti-6242. *Titanium '95: Sci Technol* 1995;1116–24.
- [3] Sinha V, Mills MJ, Williams JC. Understanding the contributions of normal fatigue and static loading to the dwell fatigue in a near-alpha titanium alloy. *Metall Trans A* 2004;35A:3141–8.
- [4] Rokhlin S, Kim JY, Zoofan B.: Columbus OH, OSU, unpublished research, 2004.
- [5] Imam MA, Gilmore CM. Room temperature creep of Ti-6Al-4V. *Metall Trans A* 1979;10A:419–25.
- [6] Sinha V, Mills MJ, Williams JC. Crystallography of Fracture facets in a near alpha titanium alloy. *Metall Trans A* 2006;37A:2015–26.
- [7] Bache MR, Evans WJ, Davies HM. Electron back scattered diffraction (EBSD) analysis of quasi-cleavage and hydrogen induced fractures under cyclic and dwell loading in titanium alloys. *J Mater Sci* 1997;32:3435–42.
- [8] Bache MR. A review of dwell sensitive fatigue in titanium alloys: the role of microstructure, texture and operating conditions. *Int J Fatigue* 2003;25:1079–87.
- [9] Bennett VP, McDowell DL. Polycrystal orientation distribution effects on microslip in high cycle fatigue. *Int J Fatigue* 2003;25:27–39.
- [10] Morrissey R, Goh C, McDowell DL. Microstructure-scale modeling of HCF deformation. *Mech Mater* 2003;25:295–311.
- [11] Hasija V, Ghosh S, Mills MJ, Joseph DS. Modeling deformation and creep in Ti-6Al alloys with experimental validation. *Acta Mater* 2003;51:4533–49.
- [12] Deka D, Joseph DS, Ghosh S, Mills MJ. Crystal plasticity modeling of deformation and creep in polycrystalline Ti-6242. *Metall Trans A* 2005;37:1371–88.
- [13] Venkataramani G, Deka D, Ghosh S. Crystal Plasticity based FE model for understanding microstructural effects on creep and dwell fatigue in Ti-6242. *J Eng Mater Tech ASME* 2006;128:356–65.
- [14] Venkataramani G, Ghosh S, Mills MJ. A size dependent crystal plasticity finite element model for creep and load-shedding in polycrystalline titanium alloys. *Acta Mater* 2007;55:3971–86.
- [15] Neeraj T, Hou DH, Daehn GS, Mills MJ. Phenomenological and Microstructural analysis of room temperature creep in titanium alloys. *Acta Mater* 2000;48:1225–38.
- [16] Williams JC, Baggerly RG, Paton NE. Deformation behavior of HCP Ti-Al alloy single crystals. *Metall Mater Trans A* 2002;33:837–50.
- [17] Bhandari Y, Sarkar S, Groeber M, Uchic M, Dimiduk D, Ghosh S. A framework for automated 3D microstructure analysis & representation. *Comp Mater Sci* 2007;41:222.
- [18] Groeber MA, Ghosh S, Uchic MD, Dimiduk DM. A Framework for automated analysis and simulation of 3D polycrystalline microstructures, Part 2: Synthetic structure generation. *Acta Mater* 2008;56:1274–87.
- [19] Groeber MA. Development of an automated characterization–representation framework for the modeling of polycrystalline materials in 3D. PhD dissertation. Columbus (OH): OSU; 2007.
- [20] Smith E. 'Dislocations and cracks', in dislocations in solids. In: Nabarro FRN, editor. Amsterdam, The Netherlands: North Holland Publishing Company; 1979.
- [21] Huang Y, Qu S, Hwang KC, Li M, Gao H. A Conventional theory of mechanism-based strain gradient plasticity. *Int J Plasticity* 2004;20:753–82.
- [22] Sinha V, Spowart JE, Mills MJ, Williams JC. Observations on the faceted initiation site in the dwell-fatigue tested Ti-6242 alloy: crystallographic orientation and size effects. *Metall Mater Trans A* 2006;37A:1507–18.
- [23] Williams et. al, FAA report summary, The Ohio State University, Columbus OH; 2006.
- [24] Venkataramani G, Kirane K, Ghosh S. Microstructural parameters affecting creep induced load shedding in Ti-6242 by a size dependent crystal plasticity FE model. *Int J Plasticity* 2008;24:428–54.
- [25] Stroh AN. The formation of cracks as a result of plastic flow. *Proc Roy Soc Lond (Ser A)* 1954;223:404–14.
- [26] Deruyttere AE, Greenough GB. The cleavage fracture of zinc single crystals. *Nature Lond* 1953;172:170–1.
- [27] Smith E. Cleavage fracture in mild steel. *Acta Mater* 1966;14:985–9.
- [28] Chan KS. A microstructure-based fatigue crack-initiation model. *Metall Mater Trans A* 2003;34:43–58.
- [29] Tanaka K, Mura T. A dislocation model for fatigue crack initiation. *J App Mech* 1981;48:97–103.
- [30] Simkin BA, Crimp MA, Bieler TR. A factor to predict microcrack nucleation at  $\gamma$ - $\gamma$  grain boundaries in TiAl. *Scripta Mater* 2003;49:149–54.
- [31] Baker I. Improving the ductility of intermetallic compounds by particle-induced slip homogenization. *Scripta Mater* 1999;41(4):409–14.
- [32] Anderson TL. *Fracture mechanics: fundamentals and applications*. 2nd ed.. Boca Raton: CRC Press; 1995.
- [33] Gao Q, Liu HW. Characterization of the Tip field of a discrete dislocation pileup for the development of physically based micromechanics. *Metall Trans A* 1990;21A:2087–9.
- [34] Zener C. *Fracturing of metals*. Symp Proc ASM, Cleveland (OH); 1948. p. 3.
- [35] Weertman J. *Dislocations based fracture mechanics*. Singapore: World Scientific; 1996.
- [36] Camacho GT, Ortiz M. Computational modeling of impact damage in brittle materials. *Int J Solids Struct* 1996;33(20–22):2899–938.
- [37] Ruiz G, Pandolfi A, Ortiz M. Three-dimensional cohesive modeling of dynamic mixed mode fracture. *Int J Numer Method Eng* 2001;52:97–120.
- [38] Parvatareddy H, Dillard DA. Effect of mode-mixity on the fracture toughness of Ti-6Al-4V/FM-5 adhesive joints. *Int J Fract* 1999;96:215–28.
- [39] Griffith AA. The phenomenon of rupture and flow in solids. *Phil Trans Roy Soc (Lond)* 1921;A221:163–98.
- [40] Irwin GR. *Fracture*. In: Flugge S, editor. *Encyclopedia of Physics*. Elast Plastic, vol. VI. Springer-Verlag; 1958. p. 551–90.
- [41] Lardner RW. *Mathematical theory of dislocations and fracture*. Toronto, Canada: University of Toronto Press; 1974.
- [42] Phillips RB. *Crystals, defects and microstructures: modeling across scales*. Cambridge: Cambridge University Press; 2001.
- [43] Fleck NA, Hutchinson JW. A phenomenological theory for strain gradient effects in plasticity. *J Mech Phys Solids* 1993;41(12):1825–57.
- [44] Gao H, Huang Y, Nix WD, Hutchinson JW. Mechanism-based strain gradient plasticity – I: Theory. *J Mech Phys Solids* 1999;47:1239–63.
- [45] Engelen RAB, Geers MGD, Baaijens FPT. Nonlocal implicit gradient-enhanced elasto-plasticity for the modeling of softening behavior. *Int J Plastic* 2003;19:403–33.